Appl. Math. Mech. -Engl. Ed., **41**(8), 1227–1250 (2020)

APPLIED MATHEMATICS AND MECHANICS (ENGLISH EDITION)

https://doi.org/10.1007/s10483-020-2633-9

Large deflection response-based geometrical nonlinearity of nanocomposite structures reinforced with carbon nanotubes*

S. ZGHAL†, A. FRIKHA, F. DAMMAK

Laboratory of Electromechanical Systems, National Engineering
School of Sfax, University of Sfax, B. P W3038, Sfax, Tunisia

(Received Oct. 11, 2019 / Revised Apr. 10, 2020)

Abstract This paper deals with the nonlinear large deflection analysis of functionally graded carbon nanotube-reinforced composite (FG-CNTRC) plates and panels using a finite element method. Based on the first-order shear deformation theory (FSDT), the proposed model takes into account the transverse shear deformations and incorporates the geometrical nonlinearity type. A C^0 isoparametric finite shell element is developed for the present nonlinear model with the description of large displacements and finite rotations. By adopting the extended rule of mixture, the effective material properties of FG-CNTRCs are approximated with the introduction of some efficiency parameters. Four carbon nanotube (CNT) distributions, labeled uniformly distributed (UD)-CNT, FG-V-CNT, FG-O-CNT, and FG-X-CNT, are considered. The solution procedure is carried out via the Newton-Raphson incremental technique. Various numerical applications in both isotropic and CNTRC composite cases are performed to trace the potential of the present model. The effects of the CNT distributions, their volume fractions, and the geometrical characteristics on the nonlinear deflection responses of FG-CNTRC structures are highlighted via a detailed parametric study.

Key words carbon nanotube (CNT), functionally graded material (FGM), geometrical nonlinearity, large deflection

Chinese Library Classification O242
2010 Mathematics Subject Classification 70-08

1 Introduction

The modeling of the nonlinear bending behaviors of plates and shells has attracted attention of many researchers, and this concern has been twice with the discovery of advanced materials such as functionally graded materials (FGMs) and carbon nanotube-reinforced composites (CNTRCs). In fact, the implementation of carbon nanotubes (CNTs) into polymer matrix composites has predicted to have large impact on many areas of science and technology due to their superlative mechanical, thermal, electrical, and chemical characteristics which make them the ultimate candidate for composite reinforcements forming the so-called CNTRC structures.

---

* Citation: ZGHAL, S., FRIKHA, A., and DAMMAK, F. Large deflection response-based geometrical nonlinearity of nanocomposite structures reinforced with carbon nanotubes. *Applied Mathematics and Mechanics* (*English Edition*), **41**(8), 1227–1250 (2020) https://doi.org/10.1007/s10483-020-2633-9

† Corresponding author, E-mail: souhirzghal@yahoo.fr

Furthermore, these CNTRCs provide a multifunctional performance for various industries, such as aerospace, aircraft, automobile, and electrical and civil engineering[1–2]. Moreover, FGMs, which are inhomogeneous composites, are characterized by the functional gradation of their mechanical properties along the thickness direction and can be applied to CNTs via the powder metallurgy fabrication procedure[3] and form a new class of materials, known as FG-CNTRCs. As a result, many researchers studied theoretically and experimentally the mechanical behavior of such advanced materials. A good review of the latest investigation made on various aspects of the mechanical behavior of FG-CNTRC beams, plates, and shells can be found in Ref. [4].

At the same time, the availability of high performance computing resources has pushed computer modeling of progress in order to provide an accurate analysis towards structural components such as beams, plates, and shells. The finite element technique has been widely used as an efficient tool in the prediction of the mechanical behavior of various shapes of structures. As a background for understanding the modeling process, a brief review of the frequently used models for the approximation of the kinematics of shell structures is provided here. The classical shell theory (CST), which is based on the Kirchhoff-Love assumptions, constitutes a suitable choice notably for thin structures. However, this theory neglects the transverse shear deformation which is an essential parameter in modeling plates and shells. To remedy this drawback, another theory, known as the first-order shear deformation theory (FSDT), was proposed by Reissner and Mindlin, wherein the effect of the transverse shear deformation was introduced. This theory gives more accurate results when the shells become thicker, and it is simple to implement in most finite element procedures. Nevertheless, this theory faces some difficulties related generally to the introduction of the shear correction factor which is numerically prohibitive or suffers the shear-locking problem in the very thin shell limit. All the limitations of the CST and the FSDT can be overcome by the higher-order shear deformation theory (HSDT) which takes into account higher-order terms in the displacement fields. Though this theory provides accurate results, it still generates further computational time which is undesirable for such applications. Hence, a bridge between the accuracy and reasonable computational time should be assured by an efficient model. In the following, the relevant works concerning the nonlinear deflection analysis of FG-CNTRC structures are briefly presented.

Following the pioneer work of Shen[5] concerning the nonlinear bending analysis of FG-CNTRC rectangular plates under a transverse uniform or sinusoidal load in thermal environments, many authors have been inspired to conduct the nonlinear large deflection analysis of FG-CNTRCs using various finite element models and numerical solutions. In relation with this subject, Shen and his co-authors presented various works on the large deflection analysis of composite laminated and FGM plates using either the HSDT[6–9] or a semi-analytical-numerical method[10–11]. With a six-parameter shell theory, Ansari et al.[12] studied the nonlinear behavior of shells. Although accurate results were provided, the analysis was restricted only to the isotropic case and did not study advanced materials such as FGMs and FG-CNTRCs. Besides, Zhang et al.[13–14] and Zhang and Liew[15] published various papers concerning the nonlinear analysis of FG-CNTRCs with different shape forms. A detailed parametric study was achieved to trace the effects of the CNT distributions, their volume fractions, and several geometrical parameters on the nonlinear deflection responses of FG-CNTRC structures. Furthermore, Mehar and Panda[16–17] and Mehar et al.[18–19] presented various analyses of nonlinear bending and vibrational behaviors of FG-CNTRC shells under thermal loading in the framework of the higher-order kinematics. Recently, Zghal et al.[20–24] conducted various investigations on FG-CNTRC structures using a high-order model within the double director finite element shell framework which induces a high-order distribution of the displacement field and imposes a zero condition of the transverse shear deformation on top and bottom surfaces. Both linear and nonlinear aspects were highlighted via several numerical examples of plates and shells. The obtained results showed the effects of the CNT profiles, their volume fractions, and various geometrical parameters on the mechanical behavior of such structures. Moreover, Frikha et al.[25], Trabelsi et al.[26–27], and Frikha and Dammak[28] presented nonlinear analyses of FGM and FG-CNTRC shells using a refined high-order theory and a modified FSDT. Reinoso and Blazquez[29] performed a nonlinear analysis of FGMs and FG-CNTRCs using a fully integrated first-order solid shell finite element. The locking problem was treated by combining the enhanced assumed strain (EAS) and assumed natural strain (ANS) methods. Though the proposed solid shell finite element allows the prediction of nonlinear behaviors of such structures with good accuracy, it requires longer computational time in the solution procedure. Therefore, to analyze the nonlinear deflection analysis with low computational cost, an accurate finite element model should be provided. Further investigations related to the nonlinear bending and vibrational buckling analyses of FGM structures can be found in Refs. [30]–[33].

This paper focuses on the large deflection analysis of FG-CNTRC shell structures. The governing equations are elaborated within the FSDT framework taking into account the transverse shear deformations, large displacements, and finite rotations. In fact, most papers presented in the literature used the FSDT with the von-Karman assumptions or employed the three-dimensional (3D) finite solid shell elements. However, the von-Karman kinematic assumptions include only membrane forces without taking into account the nonlinear contribution of the shear part which restraints its applications to small deformations. However, the 3D finite solid shell elements are costly in the solution procedure notably for complex geometries and boundary conditions. Hence, to accurately model the large deflection responses of FG-CNTRC structures with reasonable computational time, a nonlinear FSDT is proposed here. The present formulation is free of the shear-locking problem due to its implementation with the ANS method of Ref. [34]. Equally, the proposed finite shell model is implemented with a low number of nodes (four nodes) and degrees of freedom (DOFs) which ensures its computational efficiency, and it is elaborated in the sense of directors in the space with C^0 continuity. The nonlinear contribution of the transverse shear strains is considered herein, in contrast to the standard FSDT which does not present this effect. For the mechanical properties of FG-CNTRC structures, they are estimated based on the extended rule of mixture with some efficiency parameters. Four CNT distributions called uniformly distributed (UD), FG-V, FG-O, and FG-X, which are aligned in the axial direction and functionally graded in the thickness direction of the shell structure, are performed. The results show that the developed model can be utilized for the accurate and efficient analysis for large deflection of various shapes of FG-CNTRC structures. To outline these points, the present work is organized as follows. The mathematical formulation for FG-CNTRC shells is given in Section 2, wherein the geometry, the kinematics, and the governing equations of the model are presented. The finite element formulation is shown in Section 3. Numerical results in terms of large deflection responses of FG-CNTRC square, annular ring plates, and cylindrical panels are provided in Section 4. Conclusions of this work are summarized in Section 5.

2 Mathematical formulation for FG-CNTRC shells

2.1 Material properties of FG-CNTRC shells

Various profiles for the cross sections of FG-CNTRC shells are illustrated in Fig. 1, where four types of CNT distributions are considered. The UD-CNT represents the uniform distribution, while the FG-V-CNT, the FG-O-CNT, and the FG-X-CNT denote three other distributions. For the FG-V-CNT, the CNTs are rich near the top surface of the shell. For the FG-X-CNT, the CNTs are rich near both the top and bottom surfaces. The mid-plane surface is CNT-rich for the FG-O-CNT distribution. The volume fractions of CNTs V_{CNT} for the four types of distributions are given as follows:

$$V_{\mathrm{CNT}}(z)=\begin{cases} V^*_{\mathrm{CNT}} \quad \text{for} \quad \text{UD-CNT}, \\ \left(1+2\dfrac{z}{h}\right)V^*_{\mathrm{CNT}} \quad \text{for} \quad \text{FG-V-CNT}, \\ 2\left(1-2\dfrac{|z|}{h}\right)V^*_{\mathrm{CNT}} \quad \text{for} \quad \text{FG-O-CNT}, \\ 4\dfrac{|z|}{h}V^*_{\mathrm{CNT}} \quad \text{for} \quad \text{FG-X-CNT}. \end{cases} \tag{1}$$

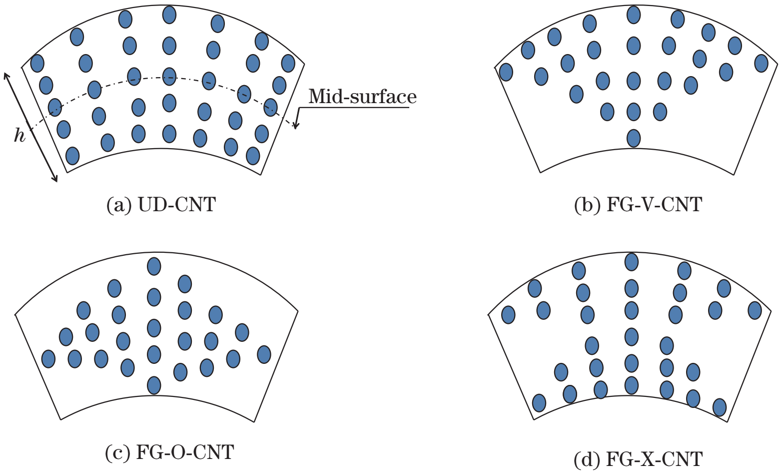

(a) UD-CNT (b) FG-V-CNT

(c) FG-O-CNT (d) FG-X-CNT

Fig. 1 Various profiles for the cross sections of FG-CNTRC shells

In Eq. (1), V^*_{CNT} denotes the total CNT volume fraction which can be expressed as

$$V^*_{\mathrm{CNT}}=\frac{w_{\mathrm{CNT}}}{w_{\mathrm{CNT}}+\frac{\rho^{\mathrm{CNT}}}{\rho^{\mathrm{m}}}-\frac{\rho^{\mathrm{CNT}}}{\rho^{\mathrm{m}}}w_{\mathrm{CNT}}}, \tag{2}$$

where ρ^{m} and ρ^{CNT} represent the mass densities of the matrix and the CNTs, respectively, and w_{CNT} is the mass fraction of CNTs. All CNT distributions have the same mass fraction w_{CNT} and a total volume fraction V^*_{CNT}. By adopting the extended rule of mixture which has improved its efficiency in the modeling of FG-CNTRC shell structures as mentioned by many researchers[5,35–36], the effective material properties of the two constituents of FG-CNTRC shell can be approximated as[5]

$$\begin{cases} E_{11}=\eta_1 V_{\mathrm{CNT}}E^{\mathrm{CNT}}_{11}+V_{\mathrm{m}}E_{\mathrm{m}}, \\ \dfrac{\eta_2}{E_{22}}=\dfrac{V_{\mathrm{CNT}}}{E^{\mathrm{CNT}}_{22}}+\dfrac{V_{\mathrm{m}}}{E_{\mathrm{m}}}, \\ \dfrac{\eta_3}{G_{12}}=\dfrac{V_{\mathrm{CNT}}}{G^{\mathrm{CNT}}_{12}}+\dfrac{V_{\mathrm{m}}}{G_{\mathrm{m}}}, \end{cases} \tag{3}$$

where E_{m} and G_{m} are Young's modulus and the shear modulus of the isotropic matrix phase, respectively, and E^{CNT}_{11}, E^{CNT}_{22}, and G^{CNT}_{12} are the corresponding ones of the CNTs. V_{m} stands for the volume fraction of the matrix and is evaluated by

$$V_{\mathrm{m}}=1-V_{\mathrm{CNT}}. \tag{4}$$

In Eq. (3), the coefficients η_i $(i=1,2,3)$ represent the efficiency parameters of CNTs which draw the scale-dependent material properties of CNTs. Their evaluation is achieved by matching the elastic modulus of CNTRC observed from the molecular dynamic simulations[37–38] with the numerical results obtained from the extended rule of mixture. According to the extended rule of mixture, the density ρ and Poisson's ratio ν_{12} can be calculated as follows:

$$\begin{cases} \rho = V_{\mathrm{CNT}}\rho^{\mathrm{CNT}} + V_{\mathrm{m}}\rho^{\mathrm{m}}, \\ \nu_{12} = V_{\mathrm{CNT}}^{*}\nu_{12}^{\mathrm{CNT}} + V_{\mathrm{m}}\nu_{\mathrm{m}}, \end{cases} \tag{5}$$

where ν_{12}^{CNT} and ν_{m} refer to Poisson's ratios of the CNTs and the matrix, respectively.

2.2 Nonlinear analysis of FG-CNTRCs based on the FSDT

The nonlinear analysis of FG-CNTRCs is performed here using the FSDT. The effects of the transverse shear deformations and geometrical nonlinearity are considered. The development steps of the proposed model are given in the next subsections.

2.2.1 Kinematics of the model

The position vectors of any material point q within the shell body in the reference C_0 and current C_t configurations (see Fig. 2) are denoted by $\boldsymbol{X}_q$ and $\boldsymbol{x}_q$, respectively, where $\boldsymbol{\xi} = (\xi^1, \xi^2, \xi^3)$ is the parametric curvilinear coordinate, in which $\xi^3 = z$. Their corresponding expressions are given by

$$\boldsymbol{X}_q(\xi^1, \xi^2, z) = \boldsymbol{X}_p(\xi^1, \xi^2) + z\boldsymbol{D}(\xi^1, \xi^2), \quad \boldsymbol{x}_q = \boldsymbol{x}_p + z\boldsymbol{d}, \tag{6}$$

where $z \in \left(-\frac{h}{2}, \frac{h}{2}\right)$ is the thickness coordinate of the shell. The pairs $(\boldsymbol{X}_p, \boldsymbol{x}_p)$ and $(\boldsymbol{D}, \boldsymbol{d})$ refer to the position vectors of an arbitrary point p of the mid-surface and the shell director vector in both the initial and deformed configurations, respectively.

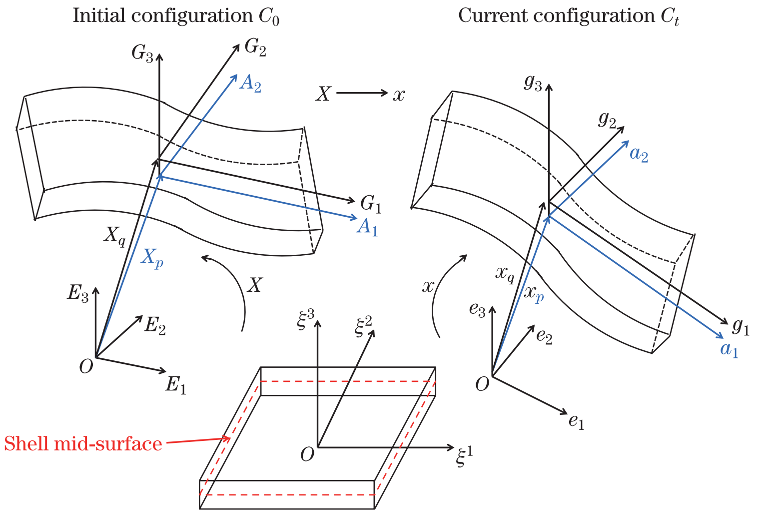

Fig. 2 Description of the shell body in the initial C_0 and deformed C_t configurations (color online)

The deformation gradient is defined according to the Green-Lagrange strain tensor field $\boldsymbol{E}$ as follows:

$$\begin{cases} E_{\alpha\beta} = e_{\alpha\beta} + z\chi_{\alpha\beta}, \quad \alpha, \beta = 1, 2, \\ \gamma_{\alpha 3} = 2E_{\alpha 3} = g_{\alpha 3} - G_{\alpha 3}, \end{cases} \tag{7}$$

where $G_{\alpha\beta}$ and $g_{\alpha\beta}$ represent the metric coefficients in both the initial C_0 and deformed C_t configurations. $e_{\alpha\beta}$, $\chi_{\alpha\beta}$, and $\gamma_{\alpha 3}$ denote the membrane, bending, and transverse shear strains, respectively, which are expressed as

$$e_{\alpha\beta} = \frac{1}{2}\left(a_{\alpha\beta} - A_{\alpha\beta}\right), \quad \chi_{\alpha\beta} = \frac{1}{2}\left(b_{\alpha\beta} - B_{\alpha\beta}\right), \quad \gamma_{\alpha 3} = \boldsymbol{a}_\alpha \cdot \boldsymbol{d} - \boldsymbol{A}_\alpha \cdot \boldsymbol{D}, \tag{8}$$

where $(A_{\alpha\beta},\ B_{\alpha\beta})$ and $(a_{\alpha\beta},\ b_{\alpha\beta})$ represent the covariant metric and curvature tensors in both the initial C_0 and deformed C_t configurations, respectively, while $\boldsymbol{A}_\alpha$ and $\boldsymbol{a}_\alpha$ are the corresponding covariant base vectors. Their expressions are given as indicated by Trabelsi et al.[26] and Frikha and Dammak[28].

Regrouping them in the matrix form, the components of the strain vectors can be written as follows:

$$\boldsymbol{e} = \begin{bmatrix} e_{11} \\ e_{22} \\ 2e_{12} \end{bmatrix}, \quad \boldsymbol{\chi} = \begin{bmatrix} \chi_{11} \\ \chi_{22} \\ 2\chi_{12} \end{bmatrix}, \quad \boldsymbol{\gamma} = \begin{bmatrix} \gamma_{13} \\ \gamma_{23} \end{bmatrix}. \tag{9}$$

2.2.2 Equilibrium equations

The governing equations are obtained from the variational principle which is based on the weak form of the equilibrium equation. Its corresponding expression is given by

$$G = \int_A (\boldsymbol{N} \cdot \delta\boldsymbol{e} + \boldsymbol{M} \cdot \delta\boldsymbol{\chi} + \boldsymbol{T} \cdot \delta\boldsymbol{\gamma}) \mathrm{d}A - G_{\mathrm{ext}} = 0, \tag{10}$$

where $\delta\boldsymbol{e}$, $\delta\boldsymbol{\gamma}$, and $\delta\boldsymbol{\chi}$ represent the variations of the shell strains, while $\boldsymbol{N}$, $\boldsymbol{M}$, and $\boldsymbol{T}$ refer to the membrane, bending, and shear stress resultants which can be expressed as follows:

$$\boldsymbol{N} = \begin{bmatrix} N^{11} \\ N^{22} \\ N^{12} \end{bmatrix}, \quad \boldsymbol{M} = \begin{bmatrix} M^{11} \\ M^{22} \\ M^{12} \end{bmatrix}, \quad \boldsymbol{T} = \begin{bmatrix} T^{13} \\ T^{23} \end{bmatrix}. \tag{11}$$

Their components are defined as follows:

$$N^{\alpha\beta} = \int_{-h/2}^{h/2} S^{\alpha\beta} \mathrm{d}z, \quad M^{\alpha\beta} = \int_{-h/2}^{h/2} z S^{\alpha\beta} \mathrm{d}z, \quad T^{\alpha 3} = \int_{-h/2}^{h/2} S^{\alpha 3}\ \mathrm{d}z, \tag{12}$$

where $S^{\alpha\beta}$ is the second Piola-Kirchhoff stress tensor. The generalized stress resultant $\boldsymbol{R}$ and strain $\boldsymbol{\Sigma}$ vectors read

$$\boldsymbol{R} = \begin{bmatrix} \boldsymbol{N} \\ \boldsymbol{M} \\ \boldsymbol{T} \end{bmatrix}, \quad \boldsymbol{\Sigma} = \begin{bmatrix} \boldsymbol{e} \\ \boldsymbol{\chi} \\ \boldsymbol{\gamma} \end{bmatrix}. \tag{13}$$

Substituting Eq. (13) into Eq. (10), the weak form of equilibrium renders

$$G(\boldsymbol{\Phi}, \delta\boldsymbol{\Phi}) = \int_A \delta\boldsymbol{\Sigma}^{\mathrm{T}} \cdot \boldsymbol{R} \mathrm{d}A - G_{\mathrm{ext}}(\boldsymbol{\Phi}, \delta\boldsymbol{\Phi}) = 0, \tag{14}$$

where $\boldsymbol{\Phi} = (\boldsymbol{u}, \boldsymbol{d})$ contains the displacement and shell vectors. The resolution of Eq. (14) is achieved via the Newton iterative algorithm, where the consistent tangent operator can be constructed by the directional derivative of the weak form in the direction of the increment $\Delta\boldsymbol{\Phi} = (\Delta\boldsymbol{u}, \Delta\boldsymbol{d})$. For the sake of convenience, the tangent operator should be divided into geometrical and material parts as

$$D_{\mathrm{G}} \cdot \Delta\boldsymbol{\Phi} = D_{\mathrm{G}} G \cdot \Delta\boldsymbol{\Phi} + D_{\mathrm{M}} G \cdot \Delta\boldsymbol{\Phi}. \tag{15}$$

2.2.3 Material constitutive laws

The material behavior is formulated through the material contribution of the tangent operator, while holding the strain constant and varying the generalized resultant of stress $\boldsymbol{R}$. This yields

$$D_{\mathrm{M}}G\cdot\Delta\boldsymbol{\Phi}=\int_{A}(\delta\boldsymbol{\Sigma}^{\mathrm{T}}\cdot\Delta\boldsymbol{R})\mathrm{d}A. \tag{16}$$

As a result, the constitutive relationships between the generalized resultant of stress $\boldsymbol{R}$ and strain $\boldsymbol{\Sigma}$ vectors are

$$\Delta\boldsymbol{R}=\boldsymbol{H}_T\Delta\boldsymbol{\Sigma}. \tag{17}$$

The material tangent modulus $\boldsymbol{H}_T$ can be expressed as follows:

$$\begin{cases}\boldsymbol{H}_T=\begin{bmatrix}\boldsymbol{H}_{\mathrm{m}} & \boldsymbol{H}_{\mathrm{mb}} & \boldsymbol{0}\\ \boldsymbol{H}_{\mathrm{mb}} & \boldsymbol{H}_{\mathrm{b}} & \boldsymbol{0}\\ \boldsymbol{0} & \boldsymbol{0} & \boldsymbol{H}_{\mathrm{s}}\end{bmatrix},\\ (\boldsymbol{H}_{\mathrm{m}},\boldsymbol{H}_{\mathrm{mb}},\boldsymbol{H}_{\mathrm{b}})=\int_{-h/2}^{h/2}\left(1,z,z^2\right)\boldsymbol{H}\mathrm{d}z,\quad \boldsymbol{H}_{\mathrm{s}}=\int_{-h/2}^{h/2}\boldsymbol{H}_{\tau}\mathrm{d}z.\end{cases} \tag{18}$$

The in-plane $\boldsymbol{H}$ and out-of-plane $\boldsymbol{H}_{\tau}$ sub-matrices are given by

$$\boldsymbol{H}=\boldsymbol{T}_1^{\mathrm{T}}\boldsymbol{H}_L\boldsymbol{T}_1,\quad \boldsymbol{H}_{\tau}=\boldsymbol{T}_2^{\mathrm{T}}\boldsymbol{H}_{\tau_L}\boldsymbol{T}_2, \tag{19}$$

where $\boldsymbol{H}_L$ and $\boldsymbol{H}_{\tau_L}$ denote the constitutive material matrices of an orthotropic single layer shell, and $\boldsymbol{T}_1$ and $\boldsymbol{T}_2$ represent the transformation matrices from the orthotropic system to the Cartesian system, as shown in Fig. 3. Their expressions are given as[23–24]

$$\boldsymbol{H}_L=\begin{bmatrix}H_{11} & H_{12} & 0\\ H_{12} & H_{22} & 0\\ 0 & 0 & G_{12}\end{bmatrix},\quad \boldsymbol{H}_{\tau_L}=\begin{bmatrix}G_{13} & 0\\ 0 & G_{23}\end{bmatrix}, \tag{20}$$

$$\boldsymbol{T}_1=\begin{bmatrix}C^2 & S^2 & CS\\ S^2 & C^2 & -CS\\ -2CS & 2CS & C^2-S^2\end{bmatrix},\quad \boldsymbol{T}_2=\begin{bmatrix}C & S\\ -S & C\end{bmatrix},\quad C=\cos\theta,\quad S=\sin\theta, \tag{21}$$

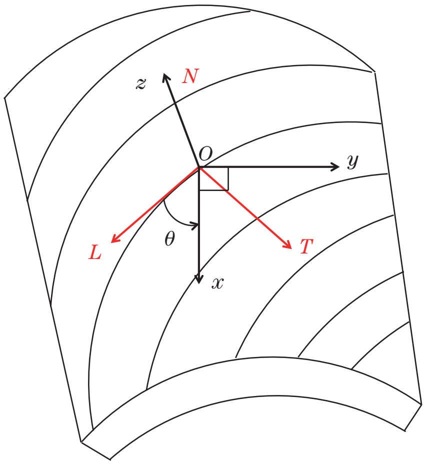

Fig. 3 Schematic of the orthotropic single layer shell (color online)

where H_{11}, H_{12}, and H_{22} are given in terms of engineering constants as follows:

$$\begin{cases} H_{11} = \dfrac{E_{11}}{\varDelta}, \quad H_{22} = \dfrac{E_{22}}{\varDelta}, \quad H_{12} = \dfrac{\nu_{21} E_{11}}{\varDelta} = \dfrac{\nu_{12} E_{22}}{\varDelta}, \\ \varDelta = 1 - \nu_{21}\nu_{12} = 1 - \nu_{12}^2 \dfrac{E_{22}}{E_{11}}, \end{cases} \tag{22}$$

where E_{11}, E_{22}, ν_{12}, ν_{21}, G_{12}, G_{13}, and G_{23} denote Young's moduli, Poisson's ratios, and the shear moduli of the single layer shell, respectively, and $G_{12} = G_{13} = G_{23}$.

2.2.4 Geometrical laws

To account for the geometrical contribution of the tangent operator, the virtual strains are varied while maintaining the stress resultant constant, which yields

$$D_{\mathrm{G}}G \cdot \Delta\boldsymbol{\Phi} = \int_A (\Delta\delta\boldsymbol{\Sigma}^{\mathrm{T}} \cdot \boldsymbol{R})\mathrm{d}A. \tag{23}$$

Now, the partition of the geometrical contribution into membrane, bending, and transverse shear parts leads to

$$D_{\mathrm{G}}G \cdot \Delta\boldsymbol{\Phi} = D_{\mathrm{G}}G_{\mathrm{m}} \cdot \Delta\boldsymbol{\Phi} + D_{\mathrm{G}}G_{\mathrm{b}} \cdot \Delta\boldsymbol{\Phi} + D_{\mathrm{G}}G_{\mathrm{s}} \cdot \Delta\boldsymbol{\Phi}. \tag{24}$$

3 Finite element formulation

In this section, the finite element formulation corresponding to the proposed nonlinear FSDT is derived. In particular, the interpolation scheme for the kinematic field is carried out by complying with the isoparametric concept and four-node shell element definition.

3.1 Interpolation of the geometry and kinematics

The discretization of the displacement vector $(\boldsymbol{u} = \boldsymbol{x} - \boldsymbol{X})$ and the shell director $\boldsymbol{d}$ can be performed through the standard isoparametric shape functions N^I as follows:

$$\delta\boldsymbol{u} = \sum_{I=1}^{4} N^I \delta\boldsymbol{u}_I, \quad \delta\boldsymbol{d} = \sum_{I=1}^{4} N^I \delta\boldsymbol{d}_I, \quad \Delta\boldsymbol{u} = \sum_{I=1}^{4} N^I \Delta\boldsymbol{u}_I, \quad \Delta\boldsymbol{d} = \sum_{I=1}^{4} N^I \Delta\boldsymbol{d}_I, \tag{25}$$

where I refers to the node of the element. The relation between the shape function derivatives in the local Cartesian and local elementary systems can be written as

$$\begin{cases} \overline{N}^I_{,1} = [\boldsymbol{J}]^{-1} N^I_{,\xi}, \\ \overline{N}^I_{,2} = [\boldsymbol{J}]^{-1} N^I_{,\eta}, \end{cases} \tag{26}$$

where $\boldsymbol{J}$ represents the Jacobian matrix which allows the transformation from $\{\boldsymbol{n}_1^0, \boldsymbol{n}_2^0\}$ to $\{\boldsymbol{A}_1, \boldsymbol{A}_2\}$ base vectors. Its expression is given by

$$\boldsymbol{J} = \begin{bmatrix} \boldsymbol{n}_1^0 \cdot \boldsymbol{A}_1 & \boldsymbol{n}_2^0 \cdot \boldsymbol{A}_1 \\ \boldsymbol{n}_1^0 \cdot \boldsymbol{A}_2 & \boldsymbol{n}_2^0 \cdot \boldsymbol{A}_2 \end{bmatrix}, \tag{27}$$

where $\boldsymbol{A}_1$ and $\boldsymbol{A}_2$ denote the covariant base vectors of the mid-surface, while the normal field $\boldsymbol{n}^0$ related to the initial configuration C_0 is defined by

$$\boldsymbol{n}^0 = \boldsymbol{A}_1 \wedge \boldsymbol{A}_2 / \left\| \boldsymbol{A}_1 \wedge \boldsymbol{A}_2 \right\|. \tag{28}$$

3.2 Transformation at the nodal level

The discretization of the displacement field in the global level is carried out via a transformation matrix $\boldsymbol{\Pi}_n$ and takes the following form:

$$\delta\boldsymbol{\Phi}_n = \boldsymbol{\Pi}_n \cdot \delta\boldsymbol{U}_n, \quad \boldsymbol{\Pi}_n = \begin{bmatrix} \boldsymbol{\Pi}_1 & \boldsymbol{0} & \boldsymbol{0} & \boldsymbol{0} \\ \boldsymbol{0} & \boldsymbol{\Pi}_2 & \boldsymbol{0} & \boldsymbol{0} \\ \boldsymbol{0} & \boldsymbol{0} & \boldsymbol{\Pi}_3 & \boldsymbol{0} \\ \boldsymbol{0} & \boldsymbol{0} & \boldsymbol{0} & \boldsymbol{\Pi}_4 \end{bmatrix}. \tag{29}$$

Each sub-matrix $\boldsymbol{\Pi}_I$ at the nodal level I is given by

$$\boldsymbol{\Pi}_I = \begin{bmatrix} \boldsymbol{I} & \boldsymbol{0} \\ \boldsymbol{0} & \boldsymbol{\Lambda} \end{bmatrix}, \quad I = 1, 2, \cdots, 4, \tag{30}$$

where $\boldsymbol{I}$ is the identity matrix, and the matrix $\boldsymbol{\Lambda}$ represents the nodal transformation which allows the passage from the director vector $\delta\boldsymbol{d}$ to the rotational DOFs $\delta\boldsymbol{\Theta}$ as follows:

$$\delta\boldsymbol{d} = \boldsymbol{\Lambda}_k \delta\boldsymbol{\Theta}, \quad \boldsymbol{\Lambda}_k = \begin{bmatrix} -\boldsymbol{t}_{2k} & \boldsymbol{t}_{1k} \end{bmatrix}_{3\times 2}. \tag{31}$$

The transformation matrix $\boldsymbol{\Lambda}$ leads to a material description with 5 DOFs/nodes which relies the generalized displacement vector $\delta\boldsymbol{\Phi}_I = \begin{bmatrix} \delta\boldsymbol{u} \\ \delta\boldsymbol{d} \end{bmatrix}_I$ to the nodal displacement vector $\delta\boldsymbol{U}_I = \begin{bmatrix} \delta\boldsymbol{u} \\ \delta\boldsymbol{\Theta} \end{bmatrix}_I$ at the nodal level I by the following expression:

$$\delta\boldsymbol{\Phi}_I = \boldsymbol{\Pi}_I \cdot \delta\boldsymbol{U}_I, \quad I = 1, 2, \cdots, 4. \tag{32}$$

All numerical examples given in Section 4 are obtained with the material description and 5 DOFs/nodes.

3.3 Interpolation of the deformations

The state of deformations, which is divided into membrane, bending, and shear parts, can be interpolated as

$$\delta\boldsymbol{e} = \boldsymbol{B}_{\mathrm{m}} \cdot \delta\boldsymbol{U}_n, \quad \delta\boldsymbol{\chi} = \boldsymbol{B}_{\mathrm{b}} \cdot \delta\boldsymbol{U}_n, \quad \delta\boldsymbol{\gamma} = \boldsymbol{B}_{\mathrm{s}} \cdot \delta\boldsymbol{U}_n, \tag{33}$$

where $\boldsymbol{B}_{\mathrm{m}}$, $\boldsymbol{B}_{\mathrm{b}}$, and $\boldsymbol{B}_{\mathrm{s}}$ are the discrete strain-displacement matrices. Their expressions are as follows:

$$\begin{cases} \boldsymbol{B}^I_{\mathrm{m}} = \begin{bmatrix} \boldsymbol{B}^I_{\mathrm{mm}} & \boldsymbol{0} \end{bmatrix}, \quad \boldsymbol{B}^I_{\mathrm{mm}} = \begin{bmatrix} \boldsymbol{n}_1^{\mathrm{T}} \overline{N}^I_{,1} \\ \boldsymbol{n}_2^{\mathrm{T}} \overline{N}^I_{,2} \\ \boldsymbol{n}_1^{\mathrm{T}} \overline{N}^I_{,2} + \boldsymbol{n}_2^{\mathrm{T}} \overline{N}^I_{,1} \end{bmatrix}, \\ \boldsymbol{B}^I_{\mathrm{b}} = \begin{bmatrix} \boldsymbol{B}^I_{\mathrm{bm}} & \boldsymbol{B}^I_{\mathrm{bb}} \boldsymbol{\Lambda}^I \end{bmatrix}, \quad \boldsymbol{B}^I_{\mathrm{bm}} = \begin{bmatrix} \boldsymbol{d}_{,1}^{\mathrm{T}} \overline{N}^I_{,1} \\ \boldsymbol{d}_{,2}^{\mathrm{T}} \overline{N}^I_{,2} \\ \boldsymbol{d}_{,1}^{\mathrm{T}} \overline{N}^I_{,2} + \boldsymbol{d}_{,2}^{\mathrm{T}} \overline{N}^I_{,1} \end{bmatrix}, \\ \boldsymbol{B}^I_{\mathrm{bb}} = \boldsymbol{B}^I_{\mathrm{mm}}, \quad \boldsymbol{B}_{\mathrm{s}} = \boldsymbol{J}^{-1} \boldsymbol{B}_{\mathrm{s}\xi}, \\ \boldsymbol{B}_{\mathrm{s}\xi} = \begin{bmatrix} N^1_{,1} \boldsymbol{d}^{\mathrm{T}}_{1B} & N^2_{,1} \boldsymbol{a}^{\mathrm{T}}_{1B} & N^2_{,1} \boldsymbol{d}^{\mathrm{T}}_{1B} & N^2_{,1} \boldsymbol{a}^{\mathrm{T}}_{1B} & N^3_{,1} \boldsymbol{d}^{\mathrm{T}}_{1D} & N^3_{,1} \boldsymbol{a}^{\mathrm{T}}_{1D} & N^4_{,1} \boldsymbol{d}^{\mathrm{T}}_{1D} & N^3_{,1} \boldsymbol{a}^{\mathrm{T}}_{1D} \\ N^1_{,2} \boldsymbol{d}^{\mathrm{T}}_{1A} & N^4_{,2} \boldsymbol{a}^{\mathrm{T}}_{2A} & N^2_{,2} \boldsymbol{d}^{\mathrm{T}}_{1C} & N^3_{,2} \boldsymbol{a}^{\mathrm{T}}_{2C} & N^3_{,2} \boldsymbol{d}^{\mathrm{T}}_{1C} & N^3_{,2} \boldsymbol{a}^{\mathrm{T}}_{2C} & N^4_{,2} \boldsymbol{d}^{\mathrm{T}}_{1A} & N^4_{,2} \boldsymbol{a}^{\mathrm{T}}_{2A} \end{bmatrix}. \end{cases} \tag{34}$$

The membrane and bending matrices are given at the nodal level I, while the shear strain is provided for all nodes using the assumed natural transverse shear strain method of Bathe1985.

A, B, C, and D are the mid-points of the element boundary set, as shown in Fig. 4, and $\boldsymbol{a}_\alpha\,(\alpha = 1, 2)$ are the covariant base vectors in the deformed configuration C_t. As a result, the variation of the generalized strain $\delta\boldsymbol{\Sigma}$ in a discrete form can be written as

$$\delta\boldsymbol{\Sigma} = \boldsymbol{B} \cdot \delta\boldsymbol{U}_n, \quad \boldsymbol{B} = \begin{bmatrix} \boldsymbol{B}_{\mathrm{m}} \\ \boldsymbol{B}_{\mathrm{b}} \\ \boldsymbol{B}_{\mathrm{s}} \end{bmatrix}. \tag{35}$$

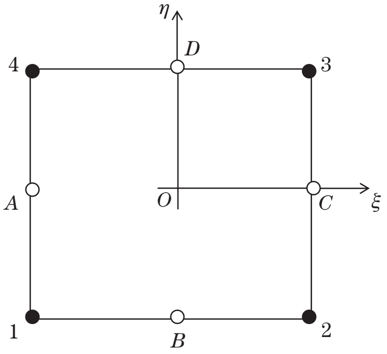

Fig. 4 The isoparametric shell element with the assumed strain construction

3.4 Solution procedure

The equilibrium equations associated to Eqs. (14) and (15) lead to the construction of the material and geometrical parts, in a discrete form, as follows:

$$\boldsymbol{K}_{\mathrm{M}} = \int_A \boldsymbol{B}^{\mathrm{T}}\boldsymbol{H}_T\boldsymbol{B}\mathrm{d}A, \tag{36}$$

$$D_{\mathrm{G}}G \cdot \Delta\Phi = \delta\Phi_n^{\mathrm{T}}\,(\boldsymbol{K}_{\mathrm{G}})\,\Delta\Phi_n = \delta\boldsymbol{U}_n^{\mathrm{T}} \cdot \boldsymbol{\Pi}_n^{\mathrm{T}} \cdot \boldsymbol{K}_{\mathrm{G}} \cdot \boldsymbol{\Pi}_n \cdot \Delta\boldsymbol{U}_n. \tag{37}$$

The expression of the geometrical matrix $\boldsymbol{K}_{\mathrm{G}}$, for a couple of nodes (I, J), is given by

$$\boldsymbol{K}_{\mathrm{G}_{IJ}} = \begin{bmatrix} UUM_{IJ}\boldsymbol{I} & (UBF_{IJ} + UBC_{IJ})\,\boldsymbol{I} \\ (BUF_{IJ} + BUC_{IJ})\,\boldsymbol{I} & (BBF_{IJ} + BBC_{IJ})\,\boldsymbol{I} \end{bmatrix}, \tag{38}$$

where UUM, (UBF, BBF), and (UBC, BBC) correspond to the membrane, bending, and shear terms, respectively, and their expressions are given as follows.

The membrane term is

$$UUM_{IJ} = \int_A \left(\overline{N}^I_{,1}\left(N^{11}\overline{N}^J_{,1} + N^{12}\overline{N}^J_{,2}\right) + \overline{N}^I_{,2}\left(N^{12}\overline{N}^J_{,1} + N^{22}\overline{N}^J_{,2}\right)\right)\mathrm{d}A. \tag{39}$$

The displacement-rotation coupling term is

$$\begin{cases} UBF_{IJ} = \int_A \left(\overline{N}^I_{,1}\left(M^{11}\overline{N}^J_{,1} + M^{12}\overline{N}^J_{,2}\right) + \overline{N}^I_{,2}\left(M^{12}\overline{N}^J_{,1} + M^{22}\overline{N}^J_{,2}\right)\right)\mathrm{d}A, \\ BUF_{IJ} = UBF_{JI}. \end{cases} \tag{40}$$

The rotation term is

$$\begin{cases} BBF_{II} = -\int_A \left(\overline{N}^I_{,1}\left(\boldsymbol{a}_1 M^{11} + \boldsymbol{a}_2 M^{12}\right) + \overline{N}^I_{,2}\left(\boldsymbol{a}_1 M^{12} + \boldsymbol{a}_2 M^{22}\right)\right)\boldsymbol{d}_I\mathrm{d}A, \\ BBF_{IJ} = 0 \quad \text{if} \quad I \neq J. \end{cases} \tag{41}$$

The shear term is

$$\boldsymbol{UBC} = \frac{1}{8}\begin{bmatrix} -\alpha-\beta & -\beta & 0 & -\alpha \\ \beta & \beta-\gamma & -\gamma & 0 \\ 0 & \gamma & \gamma+\delta & \delta \\ \alpha & 0 & -\delta & \alpha-\delta \end{bmatrix}, \tag{42}$$

$$BUC_{IJ} = UBC_{JI}, \tag{43}$$

$$\boldsymbol{BBC}_{II} = -\frac{1}{4}\begin{bmatrix} \left(\alpha \boldsymbol{a}_2^A + \beta \boldsymbol{a}_1^B\right)\cdot \boldsymbol{d}_1 \\ \left(\beta \boldsymbol{a}_1^B + \gamma \boldsymbol{a}_2^C\right)\cdot \boldsymbol{d}_2 \\ \left(\gamma \boldsymbol{a}_2^C + \delta \boldsymbol{a}_1^D\right)\cdot \boldsymbol{d}_3 \\ \left(\delta \boldsymbol{a}_1^D + \alpha \boldsymbol{a}_2^A\right)\cdot \boldsymbol{d}_4 \end{bmatrix}, \quad \boldsymbol{BBC}_{IJ} = 0 \quad \text{if} \quad I \neq J, \tag{44}$$

where

$$\begin{cases} \alpha = \int_A (1-\xi) T_2 \mathrm{d}A, & \beta = \int_A (1-\eta) T_1 \mathrm{d}A, \\ \gamma = \int_A (1+\xi) T_2 \mathrm{d}A, & \delta = \int_A (1+\eta) T_1 \mathrm{d}A. \end{cases}$$

The tangent matrix and the element residual can be written as

$$\boldsymbol{K}_T = \boldsymbol{\Pi}_n^{\mathrm{T}} (\boldsymbol{K}_{\mathrm{M}} + \boldsymbol{K}_{\mathrm{G}}) \boldsymbol{\Pi}_n, \quad \boldsymbol{r} = \int_A \boldsymbol{B}^{\mathrm{T}} \boldsymbol{R} \mathrm{d}A. \tag{45}$$

In this paper, the solution procedure is obtained by means of the Newton-Raphson incremental technique leading to the computation of nonlinear deflection responses of the studied structures.

4 Numerical applications and discussion

This section is devoted to presenting the applicability of the present formulation via the assessment of the nonlinear bending behavior of FG-CNTRC plates and curved panels. A comparison study is first carried out on the isotropic case in order to verify the capacity and the ability of the present formulation in the prediction of nonlinear deflection responses of such structures. Then, numerical applications are performed for composite structures with FG-CNT reinforcements leading to draw the usefulness and the versatility of the proposed finite element method. For FG-CNTRC simulations, Poly(m-phenylenevinylene)-co-[(2,5-dioctoxy-p-phenylene) vinylene] (PmPV) is considered for the matrix and the (10,10) armchair single walled carbon nanotubes (SWCNTs) for the reinforcements. Their corresponding material properties, at room temperature ($T = 300$ K), are $E_{11}^{\mathrm{CNT}} = 5.646\,6$ TPa, $E_{22}^{\mathrm{CNT}} = 7.080\,0$ TPa, $G_{12}^{\mathrm{CNT}} = 1.944\,5$ TPa, $\rho^{\mathrm{CNT}} = 1\,400$ kg/m^3, and $\nu_{12}^{\mathrm{CNT}} = 0.175$ for the (10,10) SWCNTs, and the values are $E_{\mathrm{m}} = 2.1$ GPa, $\rho^{\mathrm{m}} = 1\,150$ kg/m^3, and $\nu_{\mathrm{m}} = 0.34$ for the PmPV matrix[5]. Moreover, the values of the CNT efficiency parameters η_i $(i = 1, 2, 3)$ are listed in Table 1.

Table 1 Values of the CNT efficiency parameters for three sets of CNT volume fractions 11%, 14%, and 17%[5]

V_{CNT}^*	η_1	η_2	η_3
0.11	0.149	0.934	0.934
0.14	0.150	0.941	0.941
0.17	0.149	1.381	1.381

4.1 Verification and comparison study

To verify the capacity and the aptitude of the present formulation in the prediction of the nonlinear bending behavior of shell structures, several comparisons are carried out. The first numerical test consists of a simply supported square plate subject to a uniform transverse load with a length side a and a total thickness $h = 2$ mm as illustrated in Fig. 5. Its material properties are taken as indicated in Refs. [39]–[41] with $\nu = 0.316$. For comparison purpose, the results are performed in terms of non-dimensional parameters $W = W_0/h$ and $q = \frac{q_0 a^4}{E h^4}$, where E is the isotropic Young's modulus and q_0 is the uniform transverse applied load. The whole plate is meshed using 16 × 16 of S4 finite elements, where the abbreviation S4 refers to the developed nonlinear FSDT element. The non-dimensional load-deflection curves are depicted in Fig. 6. The comparison of the present curve to the one derived by Lei et al.[39] reveals a good agreement between the results, which leads to verify the aptitude of the present formulation in the prediction of nonlinear bending behavior of isotropic square plates.

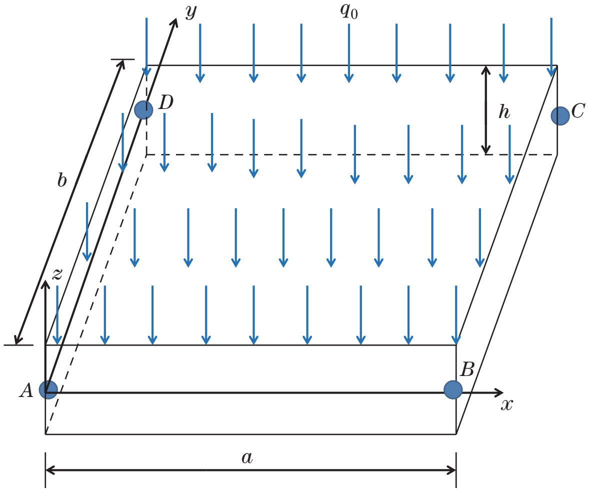

Fig. 5 The geometry of the plate

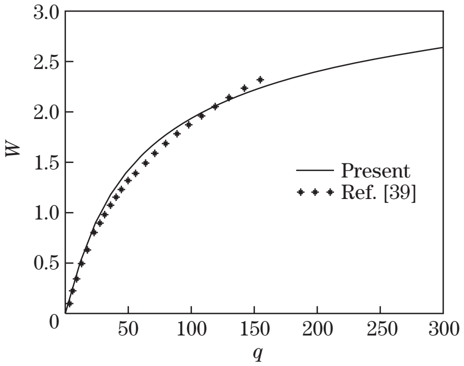

Fig. 6 Non-dimensional load-deflection curves of a simply supported square isotropic plate subject to a uniform transverse load

The second numerical test consists of an annular ring plate with a slit cut along its radial direction corresponding to the line AB as depicted in Fig. 7(a). The geometrical parameters of the ring are defined as follows: the internal radius $r = 6$ m, the external radius $R = 10$ m, and the shell thickness $h = 0.03$ m. Its material properties corresponding to the isotropic material law are Young's modulus $E = 2.1 \times 10^8$ kN/m^2 and Poisson's ratio $\nu = 0$. The ring plate is loaded at its free edge, while the other edge is fully clamped. The maximum applied load at the free edge is fixed to $p = 0.1f$ kN/m with an applied load factor $f = 60$ to obtain the deformed geometry, as shown in Fig. 7(b). The used mesh involves 8×48 of S4 finite elements. It is worth mentioning that this numerical test is considered as a good example for testing finite element shell formulations[29,42–43]. The nonlinear load-deflection responses at points A, B, and C versus the load factor f are depicted in Fig. 8. It can be seen that an excellent agreement between the present results and those reported in Ref. [42] is illustrated, which proves the ability of the present formulation in the restitution of nonlinear behavior of annular ring plates.

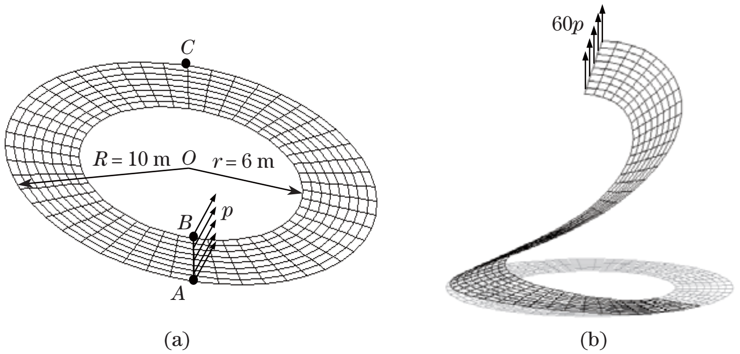

Fig. 7 The annular ring plate with (a) the geometry definition and (b) the deformed shape

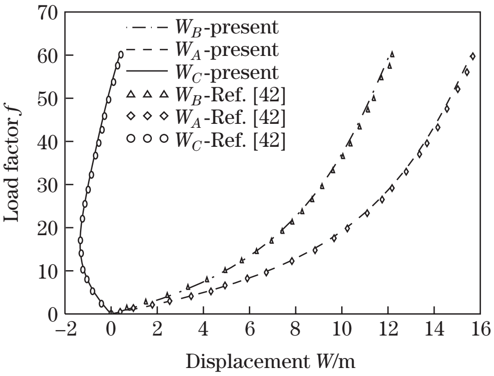

Fig. 8 Load-deflection curves of the ring plate at the load points A, B, and C

The third example considers an isotropic cylindrical panel with a concentrated transverse load at the center point of the panel, as depicted in Fig. 9. This example illustrates a shell problem and serves to test the ability of the proposed finite element to accurately reproduce the nonlinear bending behavior of curved panels. The geometrical and mechanical properties of the cylindrical panel are taken as indicated in Ref. [44], where $L = 6$ in is the axial length, $R = 2.5$ in is the radius, $\theta_0 = 45°$ is the span angle, and $h = 0.01$ in is the thickness of the shell. Young's modulus and Poisson's ratio are $E = 10^7$ psi and $\nu = 0.3$, respectively, in which 1 in =0.025 4 mm. The applied boundary condition is defined as follows. The edges AB and DC are simply supported, and the edges AD and BC are free. Due to the symmetry of the problem, only one quarter of the cylindrical panel is modeled with 10×12 meshes. Figure 10 shows a satisfactory agreement in comparison with the reference solution provided by Brendel and Ramm[44]. Thereby, the present model draws again its aptitude to perform the large deflection analysis of shell-type geometry.

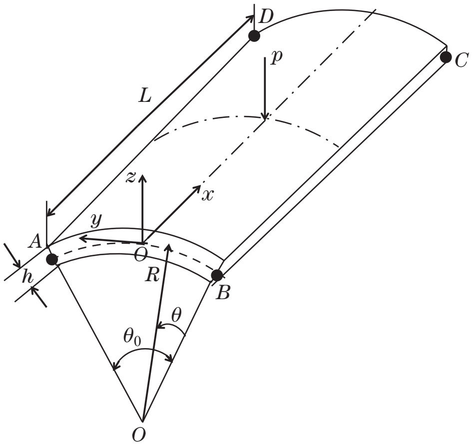

Fig. 9 The cylindrical panel under a concentrated load

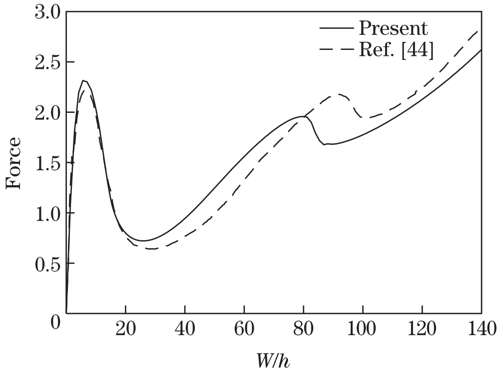

Fig. 10 Load-deflection curves of the isotropic cylindrical panel under a concentrated load

4.2 Nonlinear deflection responses of FG-CNTRC structures

To investigate the nonlinear deflection analysis of FG-CNTRC structures, parametric studies are performed in this section. Indeed, the effects of CNT profiles, their volume fractions, and some geometrical parameters including the aspect ratio, the thickness parameter, and the boundary conditions on the nonlinear bending behavior of FG-CNTRC plates and curved panels are discussed in detail through the presented numerical results. For this purpose, uniform (UD) and three graded CNT distributions, known as FG-V, FG-O, and FG-X, are considered as depicted in Fig. 1. Each configuration reflects how the CNTs are distributed through the thickness of the shell structure. In fact, for the two symmetric distributions with regard to the mid-plane surface, one can observe that the top $z = +h/2$ and the bottom $z = -h/2$ surfaces are CNT-rich for the FG-X form, and they are free of CNTs for the FG-O form. However, for the FG-V form, a maximum distribution of CNTs is displayed on the top surface $z = +h/2$, while its bottom surface $z = -h/2$ is free of CNTs. Note that for all FG-CNTRC presented structures, the geometric properties replicate those previously introduced in Subsection 5.1, whereas the material properties of the CNTs and the isotropic matrix are indicated at the beginning of Section 4.

4.2.1 Nonlinear responses of FG-CNTRC plates

Now, the applicability of the current formulation and its corresponding finite element implementation for nonlinear analysis of plates with FG-CNT reinforcements is examined. A simply supported FG-CNTRC plate under a uniform distributed load is performed. At first, for the verification purpose for FG-CNTRC plates, the non-dimensional central deflection responses of a simply supported square FG-CNTRC plate ($b/h = 50$, $V_{\mathrm{CNT}}^{*} = 0.11$) subject to a uniform transverse load and for different forms of CNTs are compared to those of Lei et al.[39] in Fig. 11. It can be seen that the present curves agree with those of Lei et al.[39] in the range [0, 100] of the non-dimensional applied load, where small deflections $W \approx 0.5$ are performed. Besides this, a difference between the results is observed due to different strategies used in the two studies. In fact, in Ref. [39], the authors used the FSDT with von-Karman kinematic assumptions including only small deformations and moderate rotations, whereas in our paper, the formulation is implemented with the introduction of large displacements and finite rotations. Hence, for a fixed load point, the present finite element model has the aptitude of the prediction of large deflections which can reach high values $W \approx 7$, while in Ref. [39], the deflections are small and do not exceed $W \approx 1.5$. Otherwise, the present results follow the shape of the curves derived by Lei et al.[39]. Therefore, the present model constitutes a more general and convenient finite element model in predicting large deflections of FG-CNTRC plates.

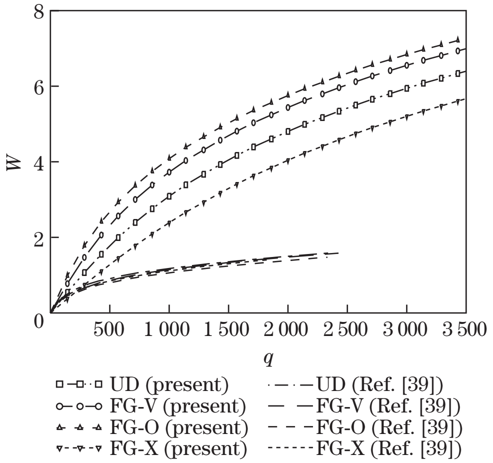

Fig. 11 Non-dimensional central deflection for various forms of simply supported square plate subject to a uniform transverse load with $b/h = 50$ and $V_{\mathrm{CNT}}^{*} = 0.11$

Figure 12 displays the effects of various profiles of CNTs on large deflection responses of a simply supported square FG-CNTRC plate ($b/h = 10$ and $V_{\mathrm{CNT}}^{*} = 0.11$) subject to a uniform transverse load. In this graph, it can be observed that the FG-O-CNT configuration is predicted to experience the largest deflection, while the FG-X-CNT case exhibits the stiffest response among different FG-CNT distributions. Moreover, the other two configurations (UD-CNT and FG-V-CNT), which are located between these extreme cases, induce a smaller central deflection for the UD form compared with the FG-V form. Hence, the CNT distributions close to the top and bottom surfaces provide a more effective reinforcement, in terms of increasing the structural stiffness of the FG-CNTRC plates. Therefore, designers can adjust the desired stiffness by choosing an appropriate form of the CNTs. In addition, Fig. 13 draws the effects of the plate aspect ratios a/b on the nonlinear central deflections of various distributions of simply supported plates with $b/h = 20$ and $V_{\mathrm{CNT}}^{*} = 0.17$ subject to a uniform transverse load. With regard to a square FG-CNTRC plate aspect ratio $a/b = 1$, two sets of aspect ratio values, less than 1, i.e., $a/b = 0.5, 0.75$, and greater than 1, i.e., $a/b = 1.5, 2$, are considered. For the former, the value of deflection is not significantly influenced by the aspect ratio, while for the latter, this effect is pronounced. In fact, for a high aspect ratio $a/b > 1$, the FG-CNTRC plate is more likely to experience the nonlinear bending than that for a lower value of the aspect ratio $a/b < 1$. Thus, the decrease in the flexural rigidity of the FG-CNTRC plate can be

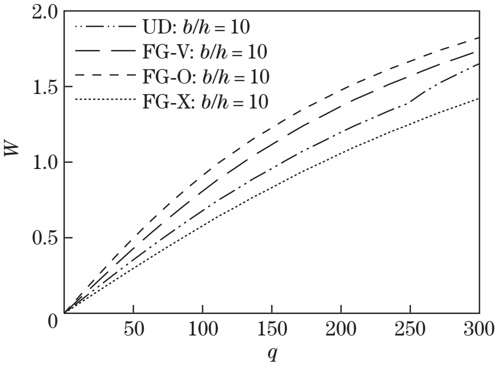

Fig. 12 Effects of various profiles of CNTs on the central large deflection responses of a simply supported square plate subject to a uniform transverse load with $b/h = 10$ and $V_{\mathrm{CNT}}^{*} = 0.11$

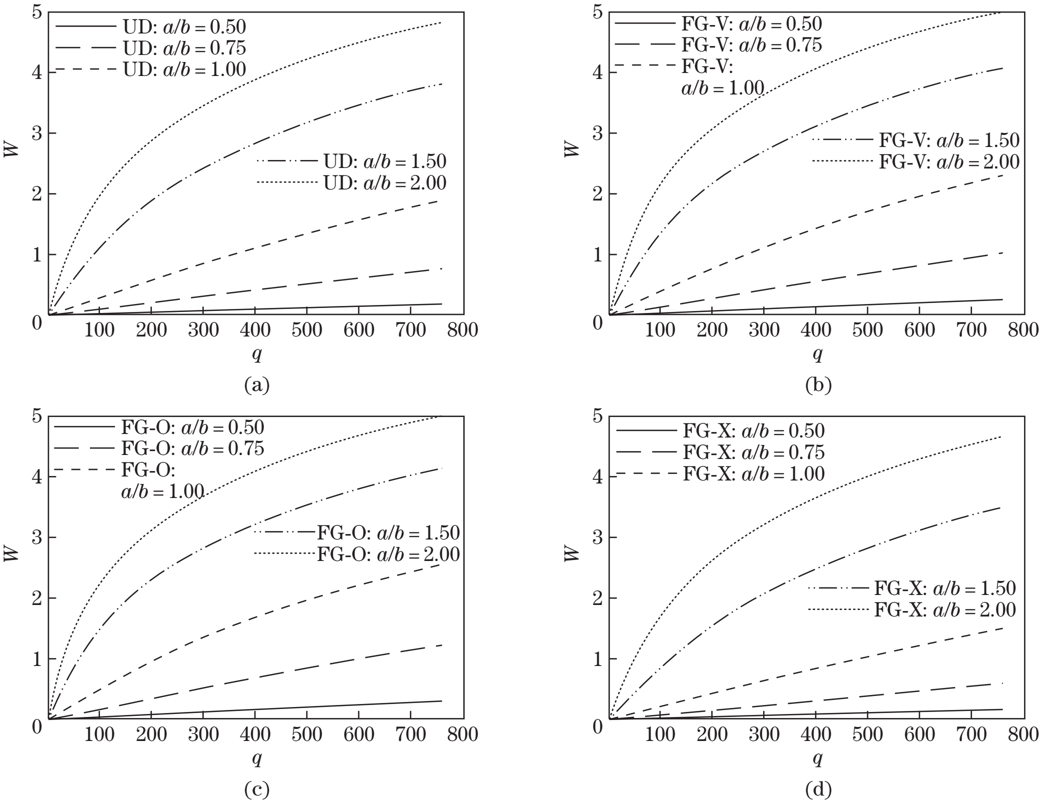

(a) (b)

(c) (d)

Fig. 13 Central large deflection responses of simply supported (a) UD-, (b) FG-V-, (c) FG-O-, and (d) FG-X-CNTRC plates subject to a uniform transverse load and under different aspect ratios with $b/h = 20$ and $V_{\mathrm{CNT}}^{*} = 0.17$

explained by the increase in the aspect ratio. Further conclusions can be deduced from Figs. 14(a), 14(b), 14(c), and 14(d) which illustrate the effects of boundary conditions on the nonlinear behavior of various forms of square FG-CNTRC plates. A sequence of boundary conditions is utilized where C, S, and F refer to clamped, simply supported, and free edge, respectively. As a result, the following combinations are examined. Four edges AB, BC, CD, and DA are fully clamped (CCCC) or fully simply supported (SSSS), a pair of opposite sides AB and DC are simply supported, and the left ones BC and AD are fully clamped or free, i.e., SCSC and SFSF, respectively. The results show that the nonlinear central deflection for a fully clamped FG-CNTRC plate is the smallest one among the four cases, while the one related to the simply supported case is the largest one. The reason is that the constraint of the clamped boundary condition is stronger than the simply supported or free boundary condition. Hence, the type of applied boundary condition has a significant effect on the nonlinear bending behavior of FG-CNTRC plates.

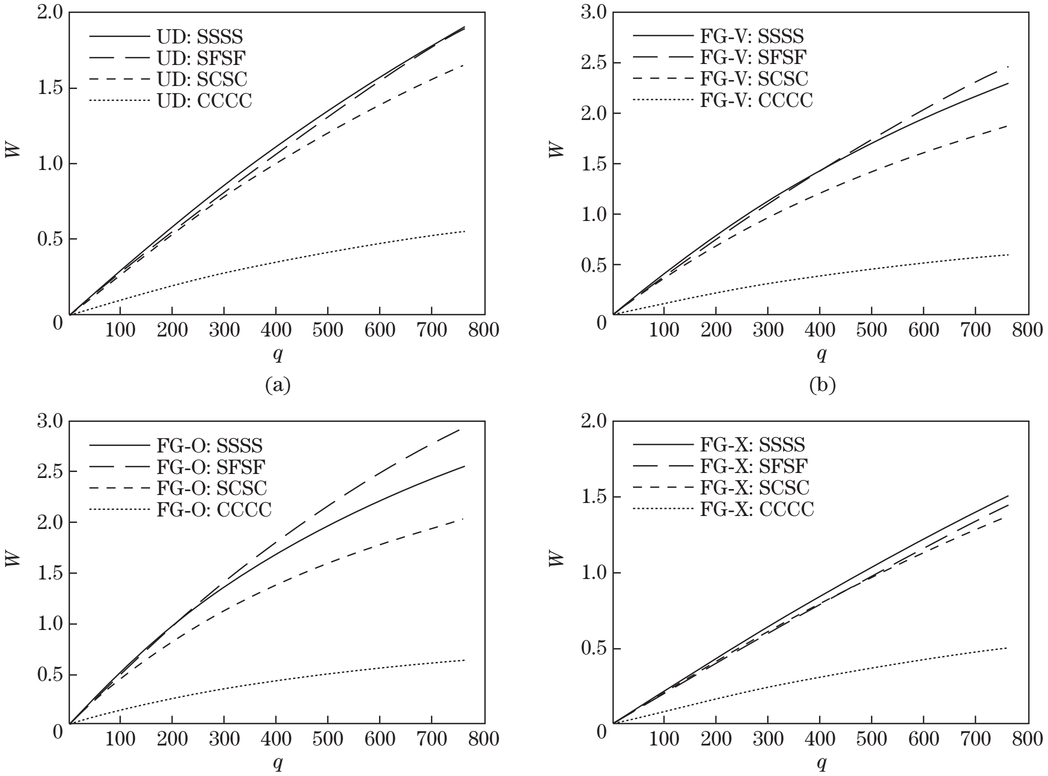

(a) (b)

(c) (d)

Fig. 14 Central large deflection responses of (a) UD-, (b) FG-V-, (c) FG-O-, and (d) FG-X-CNTRC square plates subject to a uniform transverse load and under various boundary conditions with $b/h = 20$ and $V^*_{\mathrm{CNT}} = 0.17$

4.2.2 Nonlinear responses of FG-CNTRC annular ring plates

With the same strategy, the nonlinear deflection analysis is also performed for FG-CNTRC annular ring plates. According to the existing bibliography, the large deflection analysis of FG-CNTRC annular ring plates is rather scarce. Therefore, we provide here the new first results concerning this geometry-type. First, the effects of different CNT profiles on the nonlinear bending behavior of FG-CNTRC annular ring plates are examined. Indeed, Fig. 15 depicts the load versus the vertical displacement curves at the points A, B, and C for various CNT distributions. It can be seen that the values of nonlinear deflections of FG distributions are less than those of the uniformly distribution, and this is for all load points. Consequently, FG distributions can be chosen to optimize the stiffness of the structure via the considered form of CNTs.

Furthermore, Fig. 16 shows the effects of variation of CNT volume fractions $V^*_{\mathrm{CNT}} = 0.11, 0.14, 0.17$ on nonlinear responses of UD-, FG-V-, FG-O-, and FG-X-CNTRC annular ring plates, respectively, at the studied load points. It can be observed that for a fixed load factor value f, the value of the nonlinear displacement decreases as the CNT volume fraction increases and

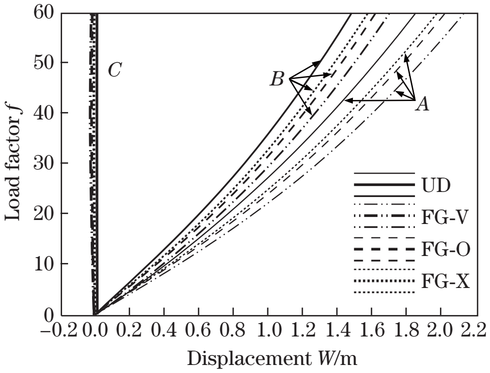

Fig. 15 Nonlinear load-displacement responses of FG-CNTRC annular ring plates at the load points A, B, and C for various CNT forms ($V^*_{\rm CNT} = 0.11$)

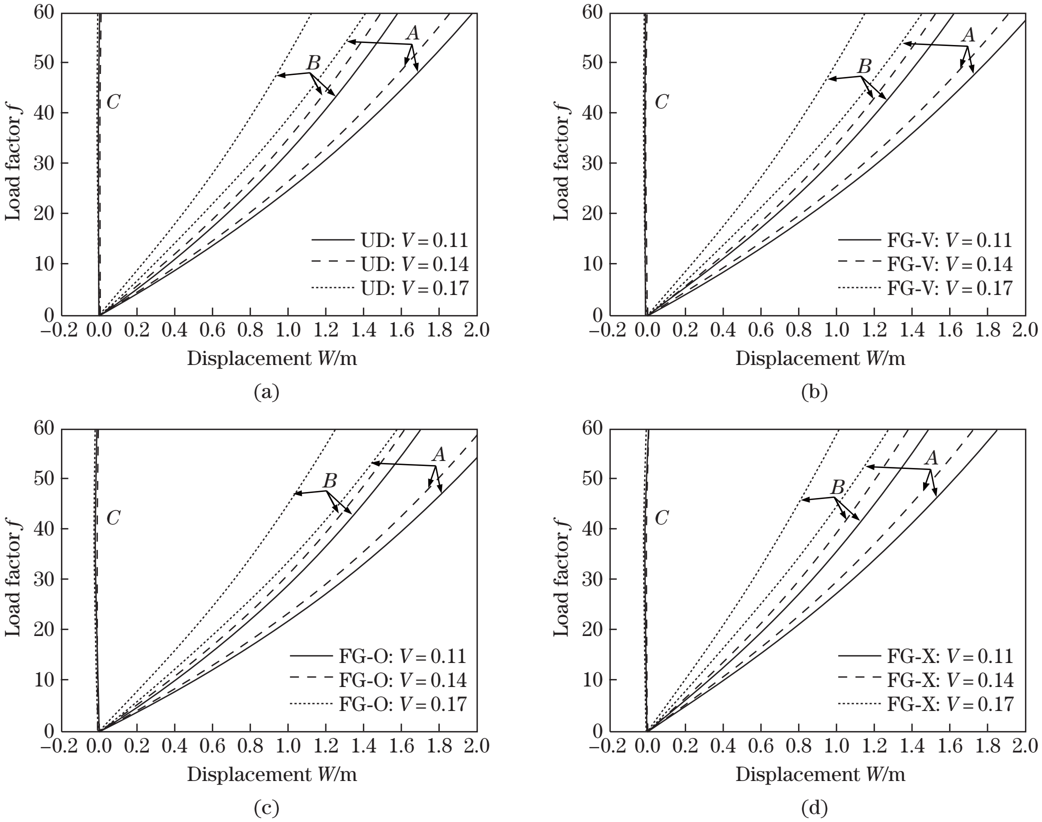

(a) (b)

(c) (d)

Fig. 16 Effects of different CNT volume fractions on large deflection responses of (a) UD-, (b) FG-V-, (c) FG-O-, and (d) FG-X-CNTRC annular ring plates at the load points A, B, and C

reaches its maximum with $V^*_{\rm CNT} = 0.17$ which implies that the more the ring plate is reinforced by CNTs, the stiffer the structure becomes. A combination between the large CNT volume fraction and the appropriate distribution of CNTs can optimize properly their bending resistance. Moreover, Fig. 17 illustrates the effects of the plate thickness parameter h on the nonlinear behavior of various forms of the FG-CNTRC ring plate at the load points A, B, and C under a CNT volume fraction $V^*_{\rm CNT} = 0.11$. The variation of the plate thickness geometrical parameter from $h = 0.01$ to $h = 0.03$ induces a decrease in the nonlinear response of the

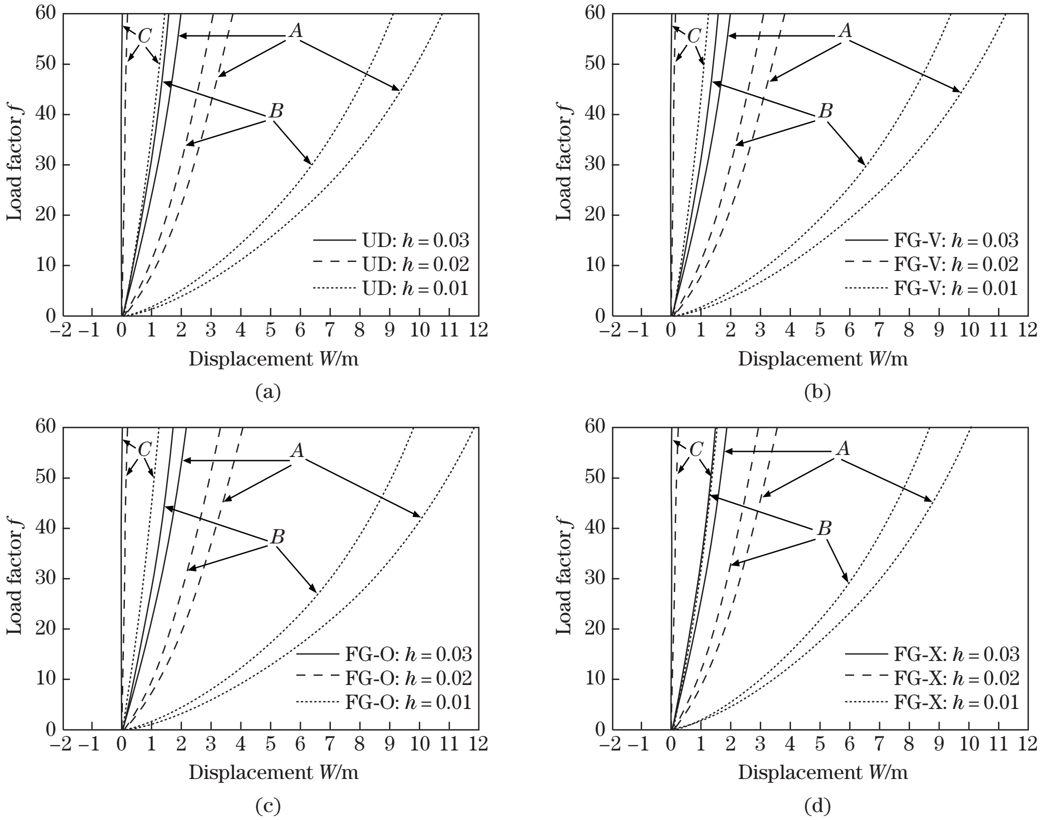

Fig. 17 Effects of the geometrical thickness parameter on large deflection responses of (a) UD-, (b) FG-V-, (c) FG-O-, and (d) FG-X-CNTRC annular ring plates at the load points A, B, and C with $V^*_{\mathrm{CNT}} = 0.11$

FG-CNTRC annular ring plate, and this is for all CNT distributions. Thus, as the thickness parameter increases, the ring plate becomes sensitive to the variation of this parameter.

4.2.3 Nonlinear responses of FG-CNTRC cylindrical panels

Finally, the nonlinear bending behavior of the FG-CNTRC cylindrical panels is investigated with a uniaxially alignment of CNTs in the axial direction and functional gradation in the thickness direction. It should be mentioned that the present results constitute the first new results for FG-CNTRC panels with a concentrated point load. In fact, most papers in the literature treated the case of FG-CNTRC panels with a uniform distributed load[13,23]. A parametric study is also carried out here to outline the effects of CNT volume fractions as well as the thickness parameter on nonlinear deflection analysis of FG-CNTRC cylindrical panels. Figures 18(a), 18(b), 18(c), and 18(d) display the effects of the CNT volume fraction, from $V^*_{\mathrm{CNT}} = 0.11$ to $V^*_{\mathrm{CNT}} = 0.17$, on the nonlinear responses of FG-CNTRC panels. The increase in the CNT volume fraction induces an increase in the stiffness of the FG-CNTRC structure which is manifested by the raise of the amplitude of the nonlinear deflection responses. Thus, the mechanical behavior of composites can be considerably improved by the addition of an appropriate percentage of CNTs. Figures 19(a), 19(b), 19(c), and 19(d) depict the load-deflection curves of UD, FG-V, FG-O, and FG-X forms, respectively. It can be remarked that as the thickness decreases, the deflection of the FG-CNTRC cylindrical panel increases. In fact, for a low value of the thickness, the FG-CNTRC cylindrical panel behaves as a thin structure and bends easily. Consequently, the variation of the thickness parameter has a significant effect on the nonlinear behavior of FG-CNTRC shell structures.

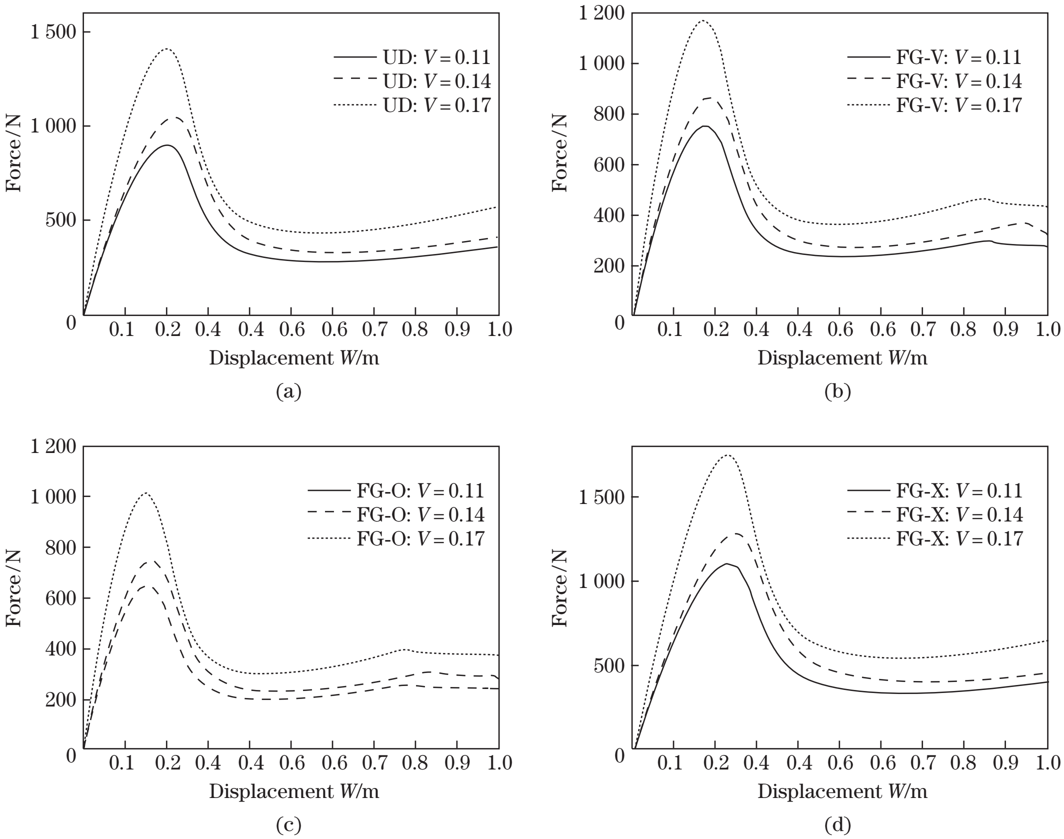

(a) (b) (c) (d)

Fig. 18 Effects of different CNT volume fractions on large deflection responses of (a) UD-, (b) FG-V-, (c) FG-O-, and (d) FG-X-CNTRC cylindrical panels

5 Conclusions

A nonlinear formulation based on the FSDT is proposed to model large deflection responses of FG-CNTRC structures. The proposed model incorporates the transverse shear deformations, and it is free of the shear-locking problem via the utilization of the ANS method. The geometrical nonlinearity type is also introduced into the formulation to accurately describe large displacements and finite rotations. SWCNTs are selected as reinforcements, and four types of distributions of CNTs are considered, i.e., a uniform distribution and three kinds of FG distributions. The material properties of FG-CNTRC structures are assumed to be graded in the thickness direction and are approximated using the extended rule of mixture with some efficiency parameters. The nonlinear equilibrium equations are solved using the Newton-Raphson numerical method. The obtained results reveal the following points.

(i) The FG-X-CNT form induces less large deflection compared with other forms, which reflects that CNT distributions close to top and bottom surfaces have the ability to optimize the nonlinear behavior of FG-CNTRC structures.

(ii) The increase in the CNT volume fraction enhances the strength of the FG-CNTRC structure, which outlines the efficiency of CNT reinforcements. In fact, when the structure is enriched by CNTs, it becomes much stiffer.

(iii) The type of applied boundary condition has a significant effect on the large deflection analysis of such structures due to the flexural rigidity of the structures which becomes stiffer with fully clamped edges.

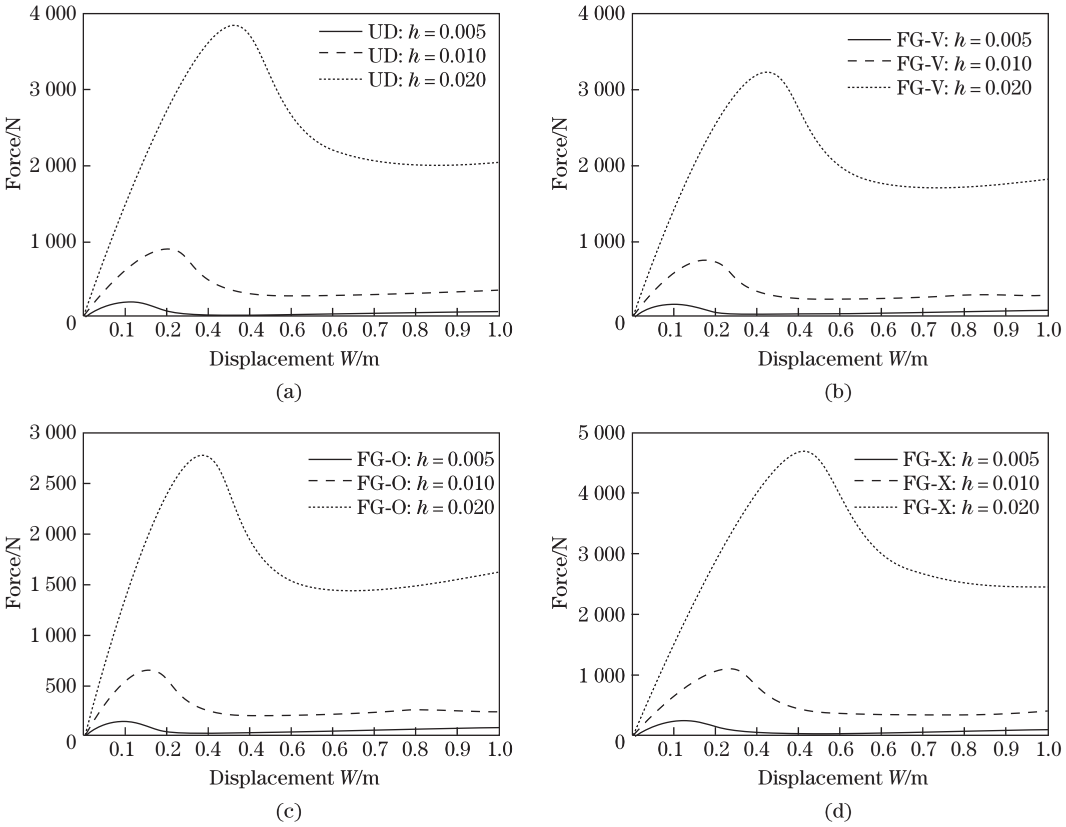

(a) (b) (c) (d)

Fig. 19 Effects of the thickness parameter on large deflection responses of (a) UD-, (b) FG-V-, (c) FG-O-, and (d) FG-X-CNTRC cylindrical panels with $V^{*}_{\mathrm{CNT}} = 0.11$

(iv) The variation of the thickness parameter induces a pronounced effect on the nonlinear behavior of FG-CNTRC structures.

(v) The proposed model allows the assessment of nonlinear behavior of FG-CNTRC plates and shells with a good presentation of large displacements and finite rotations.

References

[1] GOHARDANI, O., ELOLA, M. C., and ELIZETXEA, C. Potential and prospective implementation of carbon nanotubes on next generation aircraft and space vehicles: a review of current and expected applications in aerospace sciences. *Progress in Aerospace Sciences*, **3**, 42–68 (2014)

[2] PAL, G. and KUMAR, S. Modeling of carbon nanotubes and carbon nanotubepolymer composites. *Progress in Aerospace Sciences*, **80**, 33–58 (2016)

[3] KWON, H., BRADBURY, C. R., and LEPAROUX, M. Fabrication of functionally graded carbon nanotube reinforced aluminum matrix composite. *Advanced Engineering Materials*, **13**, 325–329 (2011)

[4] LIEW, K. M., LEI, Z. X., and ZHANG, L. W. Mechanical analysis of functionally graded carbon nanotube reinforced composites: a review. *Composite Structures*, **120**, 90–97 (2015)

[5] SHEN, H. S. Nonlinear bending of functionally graded carbon nanotube-reinforced composite plates in thermal environments. *Composite Structures*, **91**, 9–19 (2009)

[6] SHEN, H. S. and ZHANG, C. L. Non-linear analysis of functionally graded fiber reinforced composite laminated plates, part I: theory and solutions. *International Journal of Nonlinear Mechanics*, **47**, 1045–1054 (2012)

[7] SHEN, H. S. and XIANG, Y. Nonlinear analysis of nanotube-reinforced composite beams resting on elastic foundations in thermal environments. *Engineering Structures*, **56**, 698–708 (2013)

[8] SHEN, H. S. and WANG, H. Nonlinear bending of FGM cylindrical panels resting on elastic foundations in thermal environments. *European Journal of Mechanics*: *A/Solids*, **49**, 49–59 (2015)

[9] SHEN, H. S. and XIANG, Y. Nonlinear bending of nanotube-reinforced composite cylindrical panels resting on elastic foundations in thermal environments. *Engineering Structures*, **80**, 163–172 (2014)

[10] YANG, J. and SHEN, H. S. Non-linear analysis of functionally graded plates under transverse and in-plane loads. *International Journal of Non-Linear Mechanics*, **38**(4), 467–482 (2003)

[11] YANG, J. and SHEN, H. S. Nonlinear bending analysis of shear deformable functionally graded plates subjected to thermo-mechanical loads under various boundary conditions. *Composites Part B*: *Engineering*, **34**(2), 103–115 (2003)

[12] ANSARI, R., HASRATI, E., SHAKOURI, A. H., BAZDID-VAHDATI, M., and ROUHI, H. Nonlinear large deformation analysis of shells using the variational differential quadrature method based on the six-parameter shell theory. *International Journal of Non-Linear Mechanics*, **106**, 130–143 (2018)

[13] ZHANG, L. W., LEI, Z. X., LIEW, K. M., and YU, J. L. Large deflection geometrically nonlinear analysis of carbon nanotube-reinforced functionally graded cylindrical panels. *Computer Methods in Applied Mechanics and Engineering*, **273**, 1–18 (2014)

[14] ZHANG, L. W., LIU, W. H., LIEW, K. M., and YU, J. L. Geometrically nonlinear large deformation analysis of triangular CNT-reinforced composite plates. *International Journal of Non-Linear Mechanics*, **86**, 122–132 (2016)

[15] ZHANG, L. W. and LIEW, K. M. Large deflection analysis of FG-CNT reinforced composite skew plates resting on Pasternak foundations using an element-free approach. *Composite Structures*, **132**, 974–983 (2015)

[16] MEHAR, K. and PANDA, S. K. Geometrical nonlinear free vibration analysis of FG-CNT reinforced composite flat panel under uniform thermal field. *Composite Structures*, **143**, 336–346 (2016)

[17] MEHAR, K. and PANDA, S. K. Numerical investigation of nonlinear thermomechanical deflection of functionally graded CNT reinforced doubly curved composite shell panel under different mechanical loads. *Composite Structures*, **161**, 287–298 (2017)

[18] MEHAR, K., PANDA, S. K., and MAHAPATRA, T. R. Thermoelastic nonlinear frequency analysis of CNT reinforced functionally graded sandwich structure. *European Journal of Mechanics-A/Solids*, **85**, 384–396 (2017)

[19] MEHAR, K., PANDA, S. K., and MAHAPATRA, T. R. Large deformation bending responses of nanotube-reinforced polymer composite panel structure: numerical and experimental analyses. *Proceedings of the Institution of Mechanical Engineers*, *Part G*: *Journal of Aerospace Engineering*, **233**(5), 1695–1704 (2018)

[20] ZGHAL, S., FRIKHA, A., and DAMMAK, F. Static analysis of functionally graded carbon nanotube-reinforced plate and shell structures. *Composite Structures*, **176**, 1107–1123 (2017)

[21] ZGHAL, S., FRIKHA, A., and DAMMAK, F. Free vibration analysis of carbon nanotube-reinforced functionally graded composite shell structures. *Applied Mathematical Modelling*, **53**, 132–155 (2018)

[22] FRIKHA, A., ZGHAL, S., and DAMMAK, F. Dynamic analysis of functionally graded carbon nanotubes-reinforced plate and shell structures using a double directors finite shell element. *Aerospace Science and Technology*, **78**, 438–451 (2018)

[23] ZGHAL, S., FRIKHA, A., and DAMMAK, F. Non-linear bending analysis of nanocomposites reinforced by graphene-nanotubes with finite shell element and membrane enhancement. *Engineering Structures*, **158**, 95–109 (2018)

[24] ZGHAL, S., FRIKHA, A., and DAMMAK, F. Mechanical buckling analysis of functionally graded power-based and carbon nanotubes-reinforced composite plates and curved panels. *Composites Part B*: *Engineering*, **150**, 165–183 (2018)

[25] FRIKHA, A., ZGHAL, S., and DAMMAK, F. Finite rotation three and four nodes shell elements for functionally graded carbon nanotubes-reinforced thin composite shells analysis. *Computer Methods in Applied Mechanics and Engineering*, **329**, 289–311 (2018)

[26] TRABELSI, S., FRIKHA, A., ZGHAL, S., and DAMMAK, F. Thermal post-buckling analysis of functionally graded material structures using a modified FSDT. *International Journal of Mechanical Sciences*, **144**, 74–89 (2018)

[27] TRABELSI, S., FRIKHA, A., ZGHAL, S., and DAMMAK, F. A modified FSDT-based four nodes finite shell element for thermal buckling analysis of functionally graded plates and cylindrical shells. *International Journal of Mechanical Sciences*, **144**, 74–89 (2018)

[28] FRIKHA, A. and DAMMAK, F. Geometrically non-linear static analysis of functionally graded material shells with a discrete double directors shell element. *Computer Methods in Applied Mechanics and Engineering*, **150**, 1–24 (2017)

[29] REINOSO, J. and BLAZQUEZ, A. Geometrically nonlinear analysis of functionally graded power-based and carbon nanotubes reinforced composites using a fully integrated solid shell element. *Composite Structures*, **152**, 277–294 (2016)

[30] DUNG, D. V., HOA, L. K., THUYET, B. T., and NGA, N. T. Buckling analysis of functionally graded material (FGM) sandwich truncated conical shells reinforced by FGM stiffeners filled inside by elastic foundations. *Applied Mathematics and Mechanics* (*English Edition*), **37**(7), 879–902 (2016) https://doi.org/10.1007/s10483-016-2097-9

[31] DUNG, D. V. and THIEM, H. T. Mechanical and thermal postbuckling of FGM thick circular cylindrical shells reinforced by FGM stiffener system using higher-order shear deformation theory. *Applied Mathematics and Mechanics* (*English Edition*), **38**(1), 73–98 (2017) https://doi.org/10.1007/s10483-017-2159-6

[32] DUNG, D. V., NGA, N. T., and HOA, L. K. Nonlinear stability of functionally graded material (FGM) sandwich cylindrical shells reinforced by FGM stiffeners in thermal environment. *Applied Mathematics and Mechanics* (*English Edition*), **38**(5), 647–670 (2017) https://doi.org/10.1007/s10483-017-2198-9

[33] MOHAMMADIMEHR, M. and ROSTAMI, R. Bending and vibration analyses of a rotating sandwich cylindrical shell considering nanocomposite core and piezoelectric layers subjected to thermal and magnetic fields. *Applied Mathematics and Mechanics* (*English Edition*), **39**(2), 219–240 (2018) https://doi.org/10.1007/s10483-018-2301-6

[34] BATHE, K. J. and DVORKIN, E. A four-node plate bending element based on Mindlin/Reissner plate theory and a mixed interpolation. *International Journal for Numerical Methods in Engineering*, **21**, 367–383 (1985)

[35] SHEN, H. S. Postbuckling of nanotube-reinforced composite cylindrical shells in thermal environments, part I: axially-loaded shells. *Composite Structures*, **93**, 2096–2108 (2011)

[36] SHEN, H. S. and ZHANG, C. L. Thermal buckling and postbuckling behavior of functionally graded carbon nanotube-reinforced composite plates. *Materials and Design*, **31**, 3403–3411 (2010)

[37] HAN, Y. and ELLIOT, J. Molecular dynamics simulations of the elastic properties of polymer/carbon nanotube composites. *Computational Materials Science*, **39**, 315–323 (2007)

[38] ZHANG, C. L. and SHEN, H. S. Temperature-dependent elastic properties of single-walled carbon nanotubes: prediction from molecular dynamics simulation. *Applied Physics Letters*, **89**, 081904 (2006)

[39] LEI, Z. X., LIEW, K. M., and YU, J. L. Large deflection analysis of functionally graded carbon nanotube-reinforced composite plates by the element-free kp-Ritz method. *Computer Methods in Applied Mechanics and Engineering*, **256**, 189–199 (2013)

[40] GORGI, M. On large deflection of symmetric composite plates under static loading. *Journal of Mechanical Engineering Science*, **200**, 13–19 (1986)

[41] SHEN, H. S. Nonlinear bending of shear deformable laminated plates under transverse and in-plane loads and resting on elastic foundations. *Composites Structures*, **50**, 131–142 (2000)

[42] BUECHTER, N. and RAMM, E. Shell theory versus degeneration — a comparison in large rotation finite element analysis. *International Journal for Numerical Methods in Engineering*, **50**, 39–59 (1992)

[43] BUECHTER, N. and RAMM, E. On implementation of a nonlinear four node shell finite element for thin multilayered elastic shells. *Computational Mechanics*, **16**, 341–359 (1995)

[44] BRENDEL, B. and RAMM, E. Linear and nonlinear stability analysis of cylindrical shells. *Computational Mechanics*, **12**, 549–558 (1980)